

# CHAPTER FIVE

## DATA ANALYSIS AND MODEL ASSESSMENT

Initially, the effect of the antenna array configuration on the capacity is demonstrated. Figure 5.1 shows the capacity PDF at 2.4 GHz while Figure 5.2 depicts the capacity PDF at 5.2 GHz for the  $8 \times 8$  MIMO system in the same indoor location. The plots demonstrate

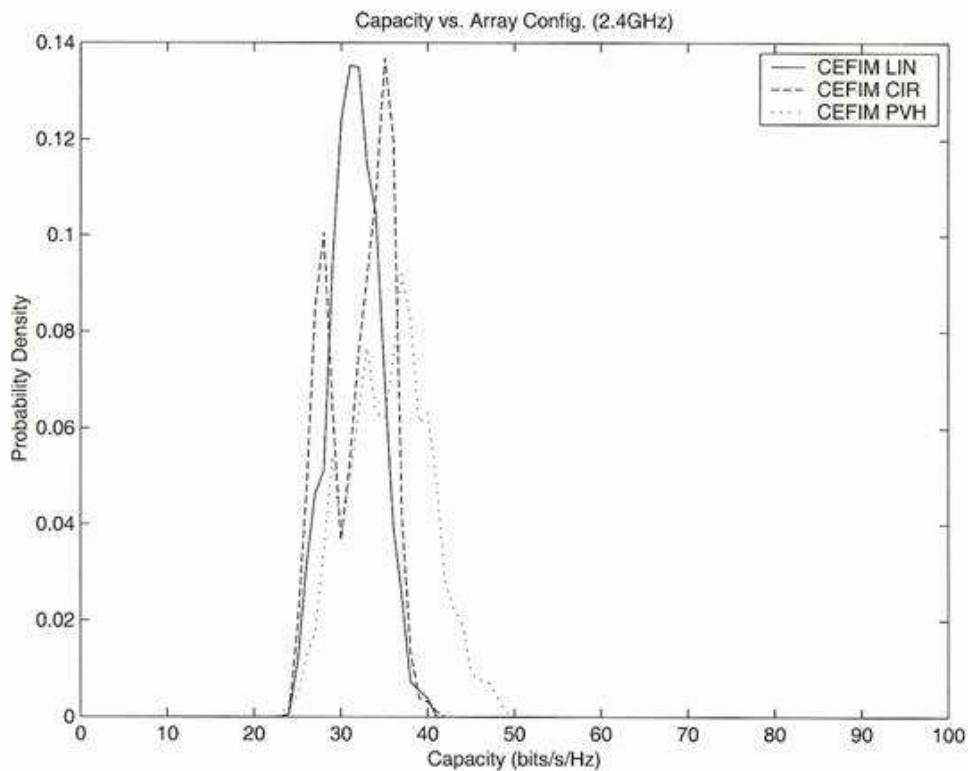


FIGURE 5.1: Capacity PDF for the MIMO system at 2.4 GHz with different array configurations

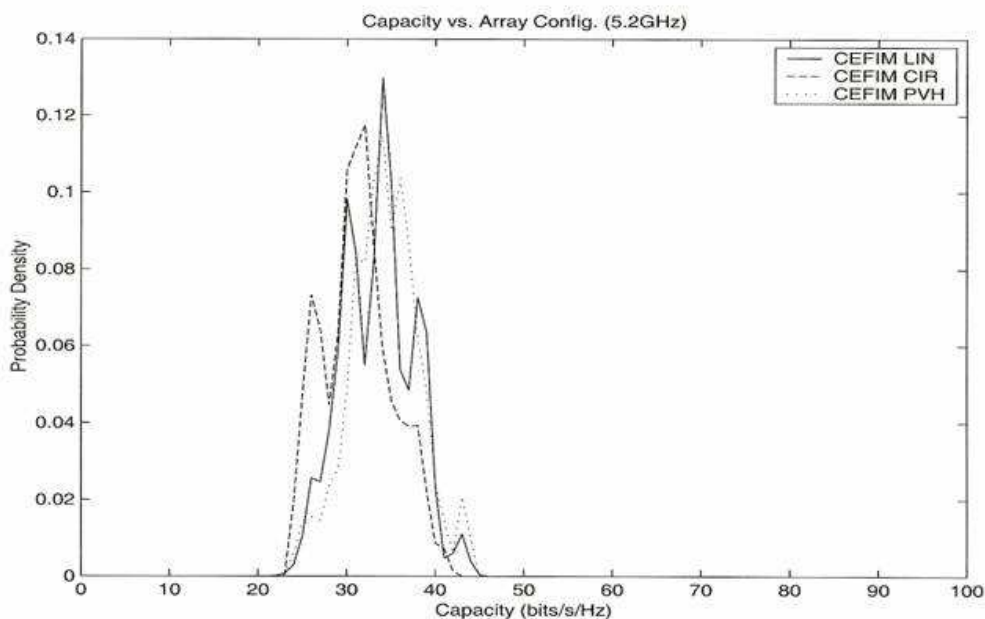


FIGURE 5.2: Capacity PDF for the MIMO system at 5.2 GHz with different array configurations

that the bulk average capacity is only weakly affected by the array configuration and that the capacity using the geometric modelling technique in Chapter 3 provides, on average, a good estimate for the indoor location.

Since the complexity of the algorithms for MIMO systems will depend on the channel rank available, it is of interest to know how much this rank depends on the target center frequency and array configuration. This dependence is investigated by plotting the cumulative distribution function (CDFs) of the channel eigenvalues over all frequency bins and all measurement locations. In Figure 5.3 the distribution at 2.4 GHz is compared with those at 5.2 GHz for the  $8 \times 8$  linear monopole arrays and in Figure 5.4 they are compared for the eight element circular array across all the physical locations. Overall, these plots show fairly weak dependence on the eigenvalue distributions on the carrier frequency, especially for the dominant eigenvalues for both the array configurations. Thus from a system standpoint, the same MIMO coding techniques will be equally applicable at the 2.4 GHz and 5.2 GHz. This result also suggests that statistical channel models that match bulk eigenvalue behavior data at 2.4 GHz can be used at 5.2 GHz.

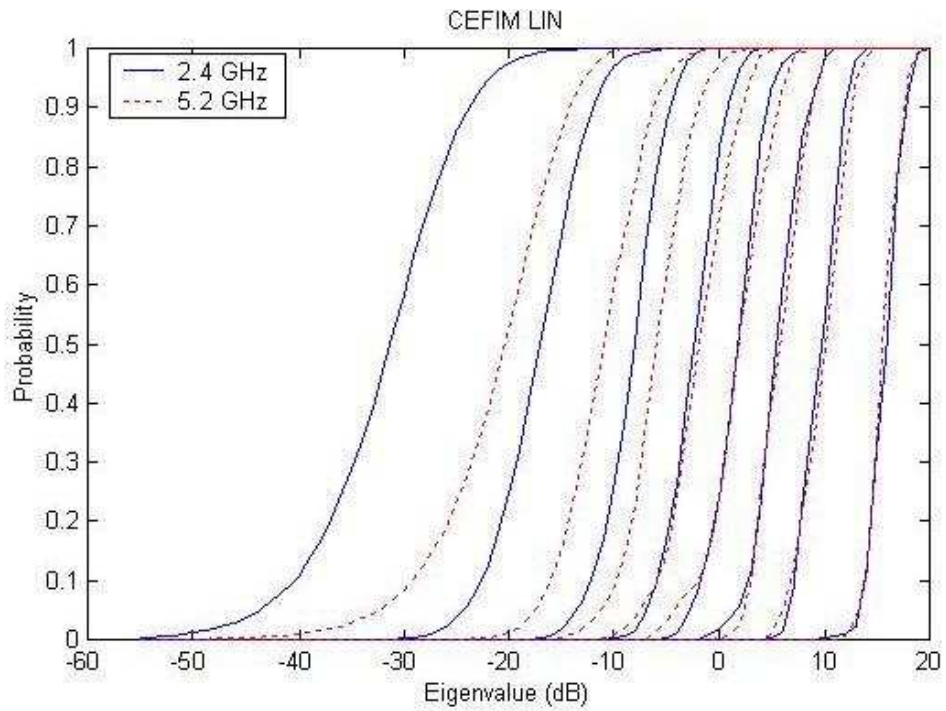


FIGURE 5.3: Eigenvalue CDFs for linear arrays at 2.4 GHz and 5.2 GHz

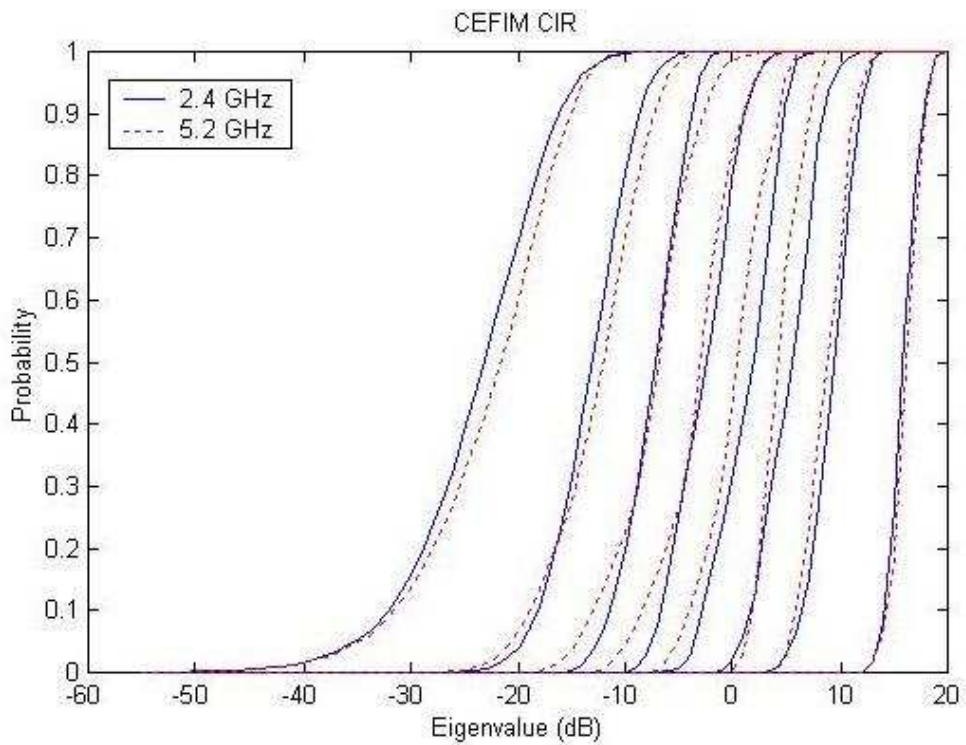


FIGURE 5.4: Eigenvalue CDFs for circular arrays at 2.4 GHz and 5.2 GHz



## 5.1 CAPACITY MODELLING

### 5.1.1 Introduction

In this section, the ability of measurements at a center frequency of 2.4 GHz is explored to predict channel behavior at a much higher center frequency of 5.2 GHz, which is referred to as frequency scaling in a MIMO system. In theory, the cost of channel measurements can be greatly reduced when such predictions are possible. Furthermore, frequency scaling suggests that MIMO techniques employed in a system with one center frequency will be directly applicable to systems operating at other frequencies, possibly decreasing the development time of MIMO systems, network planning, et cetera. The validity of frequency scaling will obviously depend on the similarity of the multi-path present at the two different frequencies. To study this idea, measurements were taken at both 2.4 GHz and 5.2 GHz at 11 site-specific measurement positions using a circular antenna array configuration. Capacities were then computed at each position for the two different center frequencies. An average pair-wise correlation measure was also applied to explain the results.

### 5.1.2 Model Description

The measurements were taken at each of the 11 locations as shown in Figure 4.21. At each of the 11 locations, 20 snapshots were recorded with 200 ms of time between snapshots. This results in a 4 s acquisition time, and since the channel sounding was for a fixed T and RX case, negligible channel variation was observed across this duration.

To remove the effect of path loss in our computations, channel matrices were normalized according to

$$\tilde{\mathbf{H}}^{(n)} = \left( \frac{1}{N_R N_T N_S} \sum_{m=1}^{N_S} \|\mathbf{H}^{(m)}\|_F^2 \right)^{-1/2} \mathbf{H}^{(n)} \quad (5.1)$$

where  $\tilde{\mathbf{H}}^{(n)}$  and  $\mathbf{H}^{(n)}$  are the  $n^{th}$  normalized and un-normalized channel matrices respectively.  $N_s$  is the number of channel measurements (snapshots and frequency bins) at a single location and  $\|\cdot\|_F$  is the Frobenius norm.

The channel capacity is computed according to the uninformed transmit capacity from [15]



as

$$C = \log_2 \det \left( I + \frac{\rho}{N_T} \tilde{\mathbf{H}} \tilde{\mathbf{H}}^H \right), \quad (5.2)$$

where  $I$  is the 8x8 identity matrix,  $\rho$  is an assumed average SISO signal to noise ratio (SNR),  $N_T$  is the number of TX antennas,  $\tilde{\mathbf{H}}$  is the normalized channel matrix and  $(\cdot)^H$  is the conjugate matrix transpose.

Across the 80 MHz excitation bandwidth for each location (loc), the average channel capacity,  $\bar{C}_{loc}$ , is determined by

$$\bar{C}_{loc} = \left( \sum_{k=1}^K C_k \right) / K, \quad (5.3)$$

where  $K=80$  is the number of discrete frequency bins and locations,  $loc = 1, \dots, 11$ .

For uniform linear arrays and far-field scattering, the correlation coefficient is shift invariant, allowing the correlation of the signals on two antennas to be presented simply as a function of the distance between elements, rather than a function of the two absolute positions of the elements. Hence in this case, the shift-invariant correlation coefficient at the RX with an element displacement of  $l$  is given as:

$$\rho_l = \frac{\left[ \sum_{k=1}^{N_S} \sum_{j=1}^{N_T} \sum_{i=1}^{N_R-l} H_{i,j}^{(k)} H_{i+l,j}^{(k)*} \right]}{\left[ \left( \sum_{k=1}^{N_S} \sum_{j=1}^{N_T} \sum_{i=1}^{N_R-l} |H_{i,j}^{(k)}|^2 \right) \left( \sum_{k=1}^{N_S} \sum_{j=1}^{N_T} \sum_{i=1}^{N_R-l} |H_{i+l,j}^{(k)}|^2 \right) \right]^{1/2}}, \quad (5.4)$$

where  $N_s=20*80$  is the number of snapshots taken across all the frequency bins and observations,  $N_T=8$  and  $N_R=8$  are the number of transmit and receiver antenna respectively, and  $H_{i,j}^{(k)}$  is the  $k^{th}$  channel snapshot from the  $j^{th}$  TX to the  $i^{th}$  RX antenna. Similarly, the shift invariant TX correlation is computed by interchanging roles of TX and RX in equation (5.4).

For the circular array no shift invariance exists, so to allow the correlation to be given in terms of a single displacement variable, the RX pairwise average absolute correlation with a displacement of  $l$  is defined as



$$\rho_l = \frac{\left\{ \sum_{i=1}^{N_R} \left| \sum_{k=1}^{N_S} \sum_{j=1}^{N_T} H(k, i, j) H^*(k, i + \ell, j) \right| \right\}}{\left[ \left\{ \sum_i^{N_R} \left| \sum_{k=1}^{N_S} \sum_{j=1}^{N_T} |H(k, i, j)|^2 \right| \right\}^{1/2} \left\{ \sum_i^{N_R} \left| \sum_{k=1}^{N_S} \sum_{j=1}^{N_T} |H(k, i + \ell, j)|^2 \right| \right\}^{1/2} \right]}. \quad (5.5)$$

In equation (5.5), the number of RX antennas,  $N_R=8$ , and number of TX antennas,  $N_T=8$ . The pairwise correlation for the TX can be computed by interchanging the roles RX and TX in equation (5.5). The only difference between this quantity and a standard correlation coefficient is the absolute value under the summation, avoiding an artificially low correlation value resulting from phase de-correlation as one moves around the array and the relative angle pair of elements rotates.

### 5.1.3 Results

Using (5.2), and for the SNR=20 dB, the ULA capacity across the 80 MHz of excitation bandwidth for each of the 11 locations shown in Figure 4.21 was calculated. From (5.4) one can also calculate the TX and RX correlation as shown in Table 5.1.

Figure 5.5 shows the capacity at location 7 both at the center frequencies of 2.4 GHz and 5.2 GHz. The model fit for the capacity at each of the center frequencies, using (5.3) is also shown in Figure 5.5. At Location 7 shown in Figure 5.5 the capacity at 5.2 GHz was found to be greater than that at 2.4 GHz, which is consistent with the correlation obtained in Table 5.1 and [97]. However, comparing this to that shown in Figure 5.6, one observes that the capacity at 2.4 GHz is greater than that at 5.2 GHz. This is consistent as seen in Table 5.1, where the correlation at 2.4 GHz is lesser than that at 5.2 GHz, both for the TX and RX cases. Except for locations 6 and 9, the average capacity across the excitation bandwidth of 80 MHz was greater at 5.2 GHz than that at 2.4 GHz, as shown in Figure 5.7 for all the 11 measured locations. At location 4 this is very marginal, and the discrepancies could be due to experimental error or not exactly positioning the RX ULA at each of these locations for each of the two center frequencies.

For the uniform circular array (UCA) configuration, using a SNR of 20 dB and using (5.2),



TABLE 5.1: TX/RX Pairwise Average Correlation of Capacity for ULA

Locations	Average Correlation ( $\rho_{av}$ )			
	2.4 GHz		5.2 GHz	
	TX	RX	TX	RX
1	0.3855	0.3600	0.2853	0.3400
2	0.3834	0.5339	0.2655	0.3271
3	0.4265	0.5301	0.2924	0.3764
4	0.0833	0.1089	0.1283	0.1520
5	0.3854	0.3740	0.2484	0.3301
6	0.3190	0.1710	0.2040	0.1364
7	0.5808	0.4041	0.3804	0.2944
8	0.1197	0.2839	0.1291	0.1257
9	0.1765	0.1721	0.5010	0.3613
10	0.3868	0.4886	0.4737	0.3743
11	0.3779	0.8617	0.3139	0.4664

the capacity across the channel excitation bandwidth can be obtained. Figure 5.9 shows the capacity at Location 9 for the 2.4 GHz and 5.2 GHz cases. The average capacity at 2.4 GHz and 5.2 GHz is obtained using (5.3) and plotted as the straight lines shown in Figure 5.9. One observes that the average capacity at 2.4 GHz is greater than that at 5.2 GHz.

The capacity for each of the 11 locations was calculated and averaged across frequency to obtain the capacities shown in Figure 5.10. One observes that in most cases the capacity at 2.4 GHz is larger than that at 5.2 GHz, most likely due to more scattering and less path loss at the lower frequency. As in [97], one should observe a lower correlation coefficient  $\rho$  for a relatively greater capacity, as verified in Tables 5.2 and 5.3. The relatively lower capacity at Locations 7 and 8 can also be explained in terms of the pairwise average correlation calculated using equation 5.5. At these locations, the correlation shown in Tables 5.2 and 5.3 for both the RX and TX antenna elements respectively, was found to be larger at 2.4 GHz than at 5.2 GHz. Furthermore Tables 5.3 and 5.2 also show that the percentage error in the determination of this pairwise correlation was a maximum of 0.5% at the RX and 2.0% at the TX, respectively, indicating that this is a reasonably reliable metric.

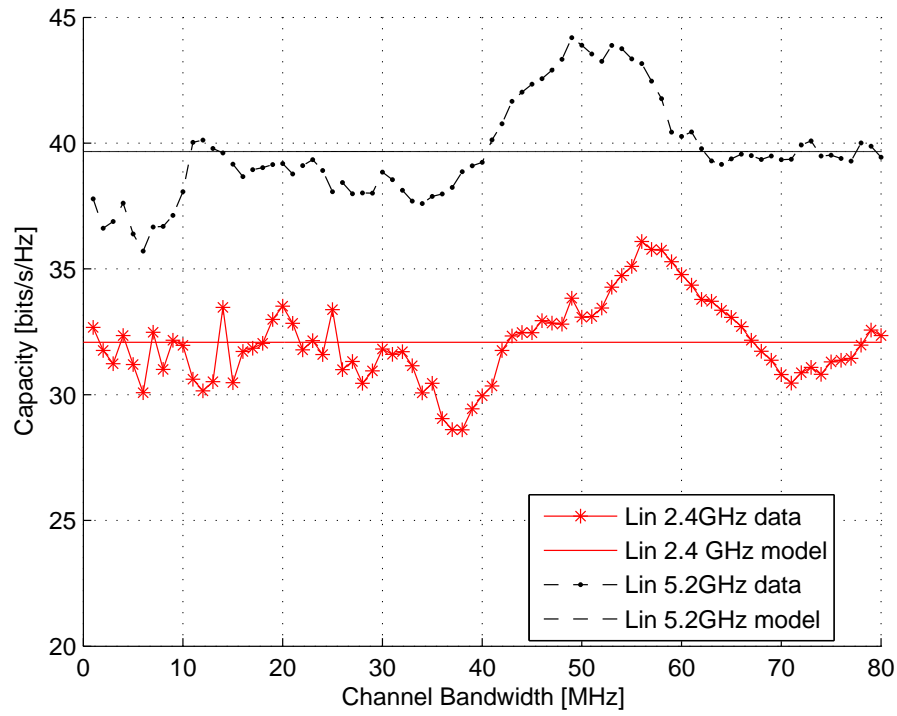


FIGURE 5.5: Capacity versus excitation bandwidth at location 7 for ULA

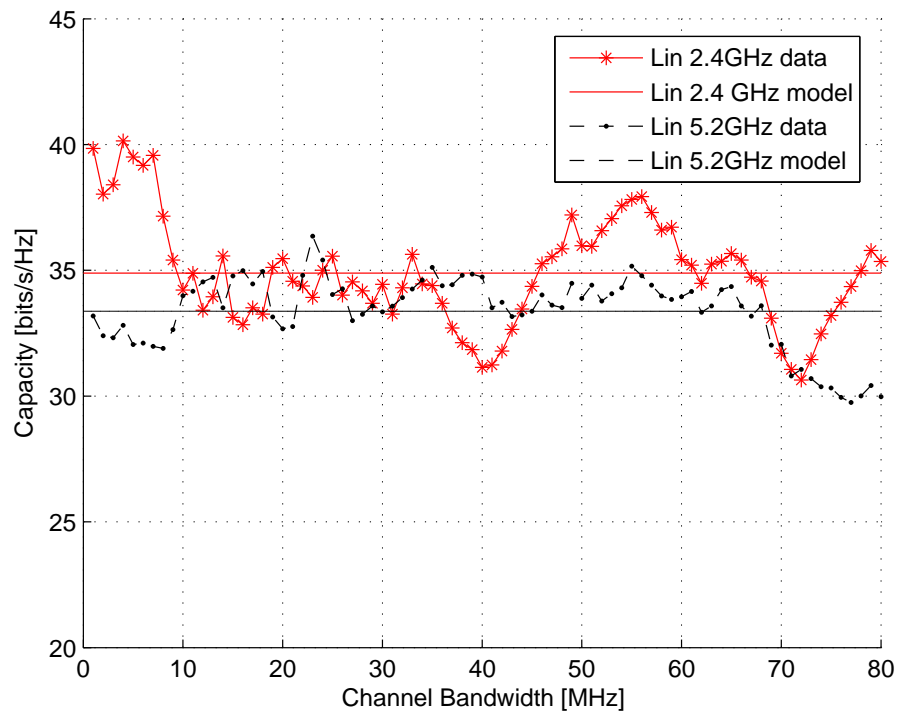


FIGURE 5.6: Capacity versus excitation bandwidth at location 9 for ULA

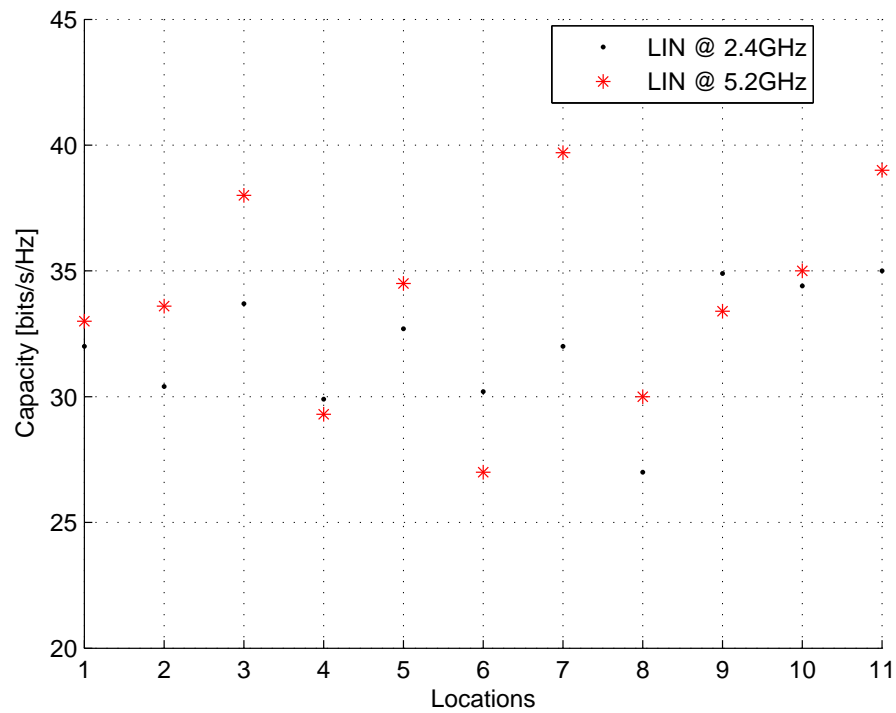


FIGURE 5.7: Average capacity at each of the measurement locations using ULA

To test the correlation of the channel capacity at the two different frequencies, Figure 5.11 presents a scatter plot of the capacities across the 11 locations at 2.4 GHz and 5.2 GHz. The solid line in the figure shows the best-fit linear dependence, obtained with the least-squares approximation. Using all the locations plotted in Figure 5.11 the straight line equation is determined to be

$$\text{cap}_{5.2} = 0.899 \times \text{cap}_{2.4} + 2.367, \quad (5.6)$$

where  $\text{cap}_{5.2}$  is the capacity at 5.2 GHz and  $\text{cap}_{2.4}$  is the capacity at 2.4 GHz respectively. The linear fit model, when all locations are considered and when Location 7 is taken as an outlier result in a variance of 3.427 and 1.905 respectively, indicating a high degree of correlation in the capacities at the two center frequencies.

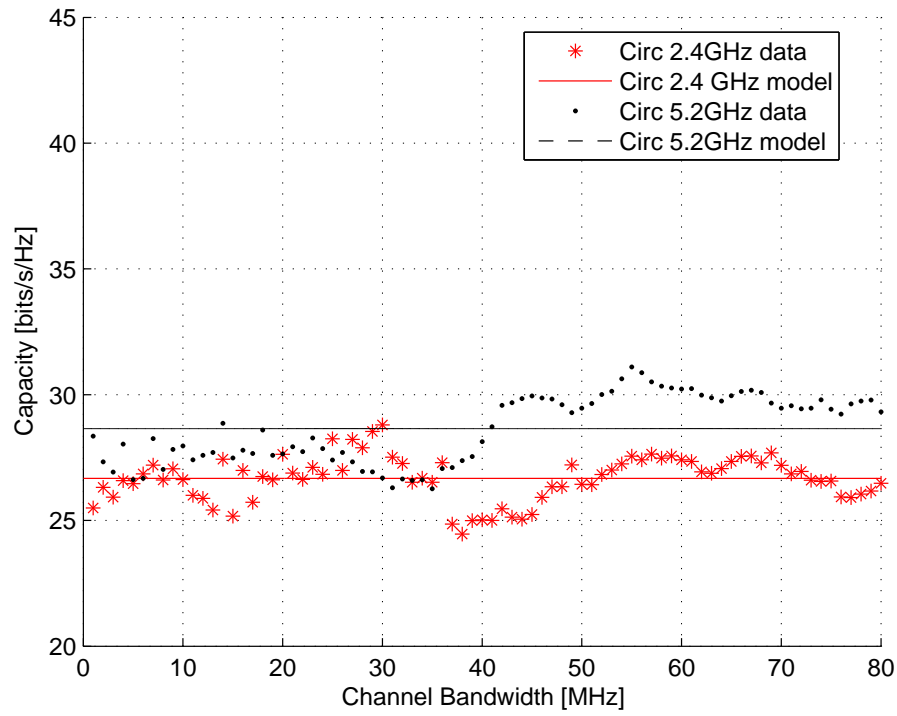


FIGURE 5.8: Capacity versus excitation bandwidth at location 8 for circular array

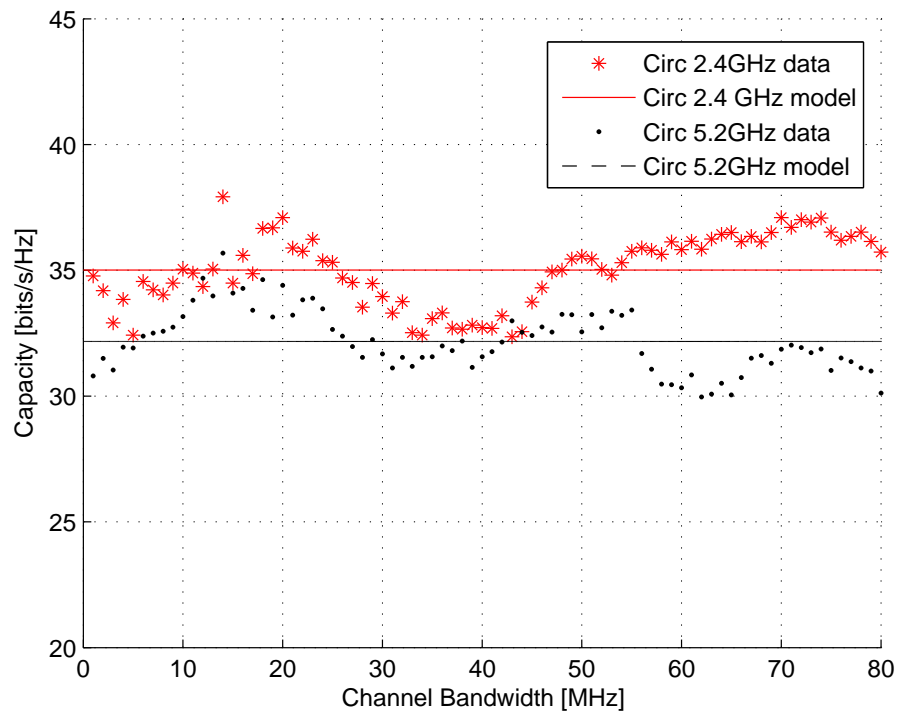


FIGURE 5.9: Capacity versus excitation bandwidth at location 9 for circular array



TABLE 5.2: TX Pairwise Average Correlation of Capacity for UCA

Locations	Transmitter (TX)			
	2.4 GHz		5.2 GHz	
	$\rho_{av}$	error(%)	$\rho_{av}$	error(%)
1	0.1646	0.95	0.1553	0.10
2	0.1510	0.83	0.1535	0.40
3	0.2126	0.63	0.2330	0.37
4	0.1449	0.98	0.1692	0.07
5	0.1767	0.64	0.1774	0.05
6	0.2191	1.92	0.2335	1.02
7	0.2292	0.46	0.1897	1.00
8	0.2306	1.46	0.2010	0.57
9	0.1922	0.21	0.1964	0.38
10	0.1545	0.77	0.1547	0.08
11	0.1910	0.66	0.1949	0.05

TABLE 5.3: RX Pairwise Average Correlation of Capacity for UCA

Locations	Receiver (RX)			
	2.4 GHz		5.2 GHz	
	$\rho_{av}$	error(%)	$\rho_{av}$	error(%)
1	0.3292	0.53	0.4824	0.22
2	0.4927	0.27	0.4531	0.04
3	0.4035	0.09	0.4505	0.14
4	0.6371	0.26	0.7174	0.14
5	0.5112	0.12	0.5797	0.41
6	0.6954	0.08	0.5887	0.32
7	0.4196	0.05	0.3758	0.33
8	0.7413	0.24	0.6349	0.18
9	0.3896	0.12	0.5357	0.37
10	0.3609	0.09	0.3635	0.53
11	0.3670	0.16	0.4561	0.02

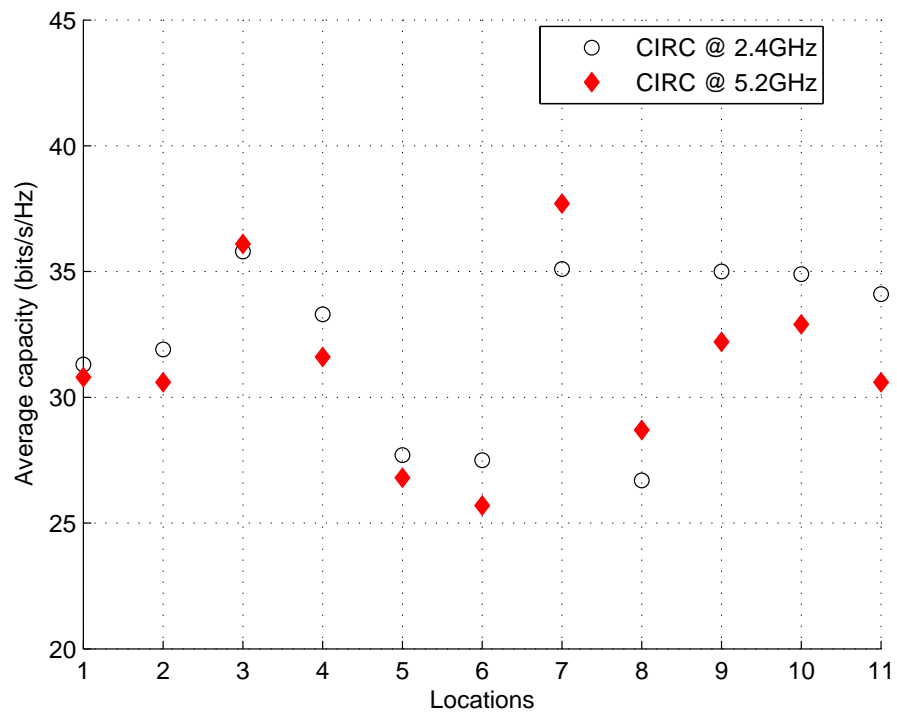


FIGURE 5.10: Average capacity at each of the measurement locations in CEFIM

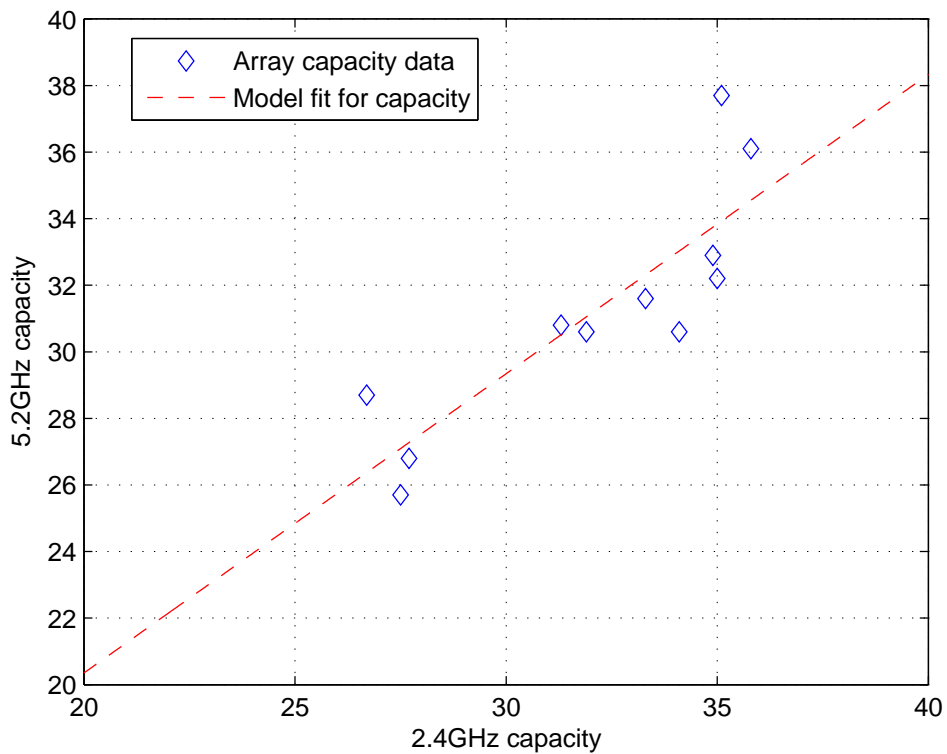


FIGURE 5.11: Frequency scaling relationship of capacities in WB indoor environment



## 5.2 MODELLING SPATIAL CORRELATION

### 5.2.1 Introduction

In this section, spatial correlation is explored at a center frequency of 2.4 GHz to predict measurements at a much higher center frequency of 5.2 GHz, which has been referred to as frequency scaling. In theory, the cost of channel measurements can be greatly reduced when such predictions are possible. Furthermore, frequency scaling suggests that MIMO techniques employed in a system with one center frequency will be directly applicable to systems operating at other frequencies, possibly decreasing the development time of MIMO systems and network planning. Obviously, the validity of frequency scaling depends on the similarity of the multipath at the two different frequencies. The modelling approach, parameter determination and the results when frequency scaling is employed using uniform linear arrays (ULA) across all the 11 measured locations are described.

### 5.2.2 Model Description

At each of the 11 locations shown in Figure 4.21, 20 channel snapshots were recorded with 200 ms between snapshots. This resulted in a 4 s acquisition time, and since the channel sounding was for a fixed TX and RX case, negligible channel variation was observed across this duration.

To remove the effect of path loss in our computations, channel matrices were normalized according to

$$\tilde{\mathbf{H}}^{(n)} = \left( \frac{1}{N_R N_T N_S} \sum_{m=1}^{N_S} \|\mathbf{H}^{(m)}\|_F^2 \right)^{-1/2} \mathbf{H}^{(n)}, \quad (5.7)$$

where  $\tilde{\mathbf{H}}^{(n)}$  and  $\mathbf{H}^{(n)}$  are the  $n^{th}$  normalized and un-normalized channel matrices respectively.  $N_s$  is the number of channel measurements (snapshots and frequency bins) at a single location and  $\|\cdot\|_F$  is the Frobenius norm.

The ULA measurements are well suited to correlation studies since the ULA has a shift-invariant correlation structure under the assumption of far-field scattering. Also in a rich multipath environment, the correlation of the ULA will depend mainly on the relative orientation of the array and the multi-path, allowing the directional signature of the multi-path



to be investigated.

For the ULA, far-field scattering produces a shift-invariant correlation structure, allowing the transmit or receive correlation to be written as a function of just the offset between elements, instead of a function of both indices. In this case, the shift-invariant correlation coefficient at the RX with an element displacement of  $l$  is

$$\rho_l = \frac{\left[ \sum_{k=1}^{N_S} \sum_{j=1}^{N_T} \sum_{i=1}^{N_R-l} H_{i,j}^{(k)} H_{i+l,j}^{(k)*} \right]}{\left[ \left( \sum_{k=1}^{N_S} \sum_{j=1}^{N_T} \sum_{i=1}^{N_R-l} |H_{i,j}^{(k)}|^2 \right) \left( \sum_{k=1}^{N_S} \sum_{j=1}^{N_T} \sum_{i=1}^{N_R-l} |H_{i+l,j}^{(k)}|^2 \right) \right]^{1/2}}, \quad (5.8)$$

where  $N_s = 20 \times 80$  is the number of snapshots taken across all frequency bins and observations,  $N_T = 8$  and  $N_R = 8$  are the number of transmit and receive antenna, respectively, and  $H_{i,j}^{(k)}$  is the  $k^{\text{th}}$  channel snapshot from the  $j^{\text{th}}$  TX to the  $i^{\text{th}}$  RX antenna. The shift-invariant TX correlation is computed by interchanging the roles of TX and RX in equation (5.8) above.

To simplify the analysis of correlation, the magnitude of  $\rho_l$  was modelled with the exponential function as

$$y_l = e^{-bl\Delta x} \quad (5.9)$$

where  $\Delta x$  is the element separation in wavelengths and  $b$  is the estimated *decorrelation* parameter, which is chosen to minimize the average mean square error (MSE),  $\bar{d}$  at TX and RX, where

$$\bar{d} = \frac{1}{\{N_T, N_R\}} \sum_{\ell=0}^{\{N_T, N_R\}-1} (|\rho_\ell| - y_\ell)^2, \quad (5.10)$$

and separate values of  $b$  are estimated at the TX and RX for each frequency.

Frequency scaling of the spatial correlation was tested by applying the linear regression technique to the decorrelation at the two frequencies, or

$$q_{5.2} = a_1 + a_2 q_{2.4}, \quad (5.11)$$

where  $q_{5.2,2.4}$  is the decorrelation at 5.2 GHz and 2.4 GHz respectively, and  $a_1$  and  $a_2$  are obtained with the minimum mean square error (MSE) curve fit.



### 5.2.3 Results

Figure 5.12 plots the shift-invariant correlation coefficient at the RX for location 4 versus antenna element displacement (in wavelengths) for both 2.4 GHz and 5.2 GHz, whilst Figure 5.14 shows the plot at the TX. The symbols and smooth lines in both plots refer to the data points and the best-fit exponential model respectively.

At location 7, where the capacities were higher in relative terms and the differential in capacity between 2.4 GHz and 5.2 GHz was greatest, one observes in Figure 5.13 that the de-correlation parameter was also correspondingly greater. Similarly, Figure 5.15 shows that the de-correlation parameter is very low at location 8, where the capacity is also lower. It was also found that one cannot use the absolute value, but the relative can be used for comparative and analytical purposes.

The RX decorrelation parameter  $b$ , as well as the MSE of the model fit to the data points for all 11 locations is computed in Table 5.4 for both the 2.4 GHz and 5.2 GHz channel data. Typical MSE of the model is between 0.2% and 3.3% with only about 20% of the locations having an error above 4%. Average error for the 2.4GHz and 5.2GHz sets are 2.34% and 2.26% respectively, indicating a remarkable good fit for the chosen model.

Following the same procedure for the TX correlation, results obtained from the decorrelation parameter values are listed in Table 5.5. Typical MSE of the model is between 0.2% and 2.9%. The average error for the 2.4 GHz and 5.2 GHz sets is 1.9% and 1.4%, again indicating a good fit for the model.

To establish the effect of frequency scaling on the decorrelation, Figure 5.16 plots the RX parameter  $b_{5.2}$  versus  $b_{2.4}$  using the data from Table 5.4. One observes that there is very high dependence present with the exception of location 9 having (0.34442, 1.2042). The broken and solid lines in Figure 5.16 show the linear regression of the data when all data points are considered and when location 9 is discarded as an outlier respectively. MSE values for these two cases are 0.109 and 0.012 respectively. Performing a linear regression of the decorrelation parameter using the data in Table 5.5 at TX as shown in Figure 5.17 results in MSE values of 0.136 and 0.034 when again location 9 is included and discarded as an outlier, respectively.

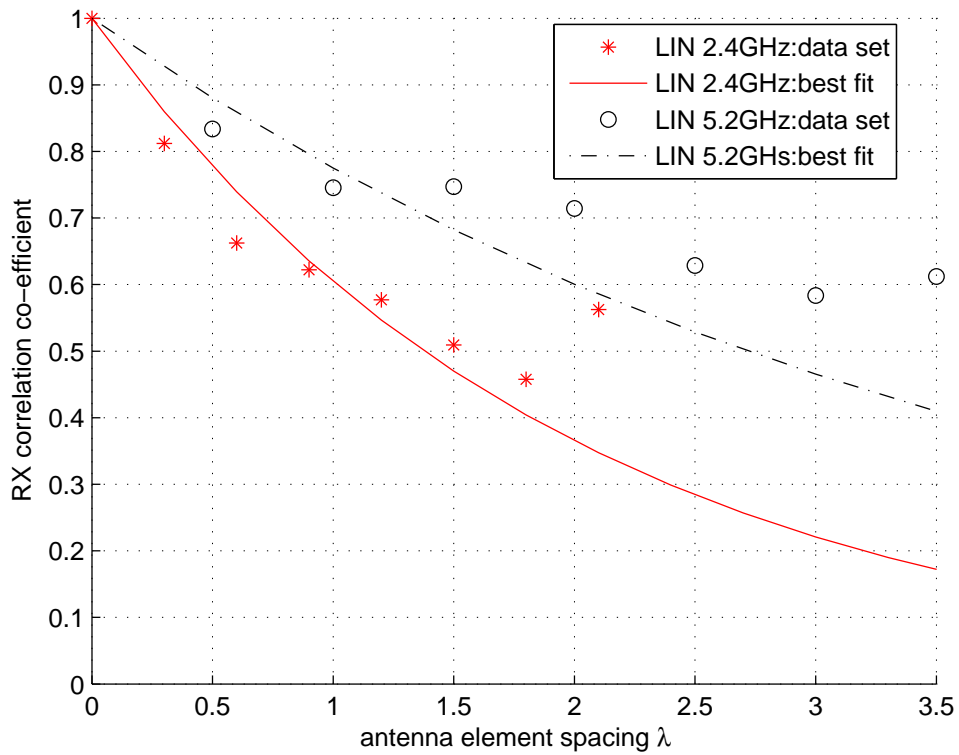


FIGURE 5.12: Calculated relative correlation coefficients with curve fit for RX location 4

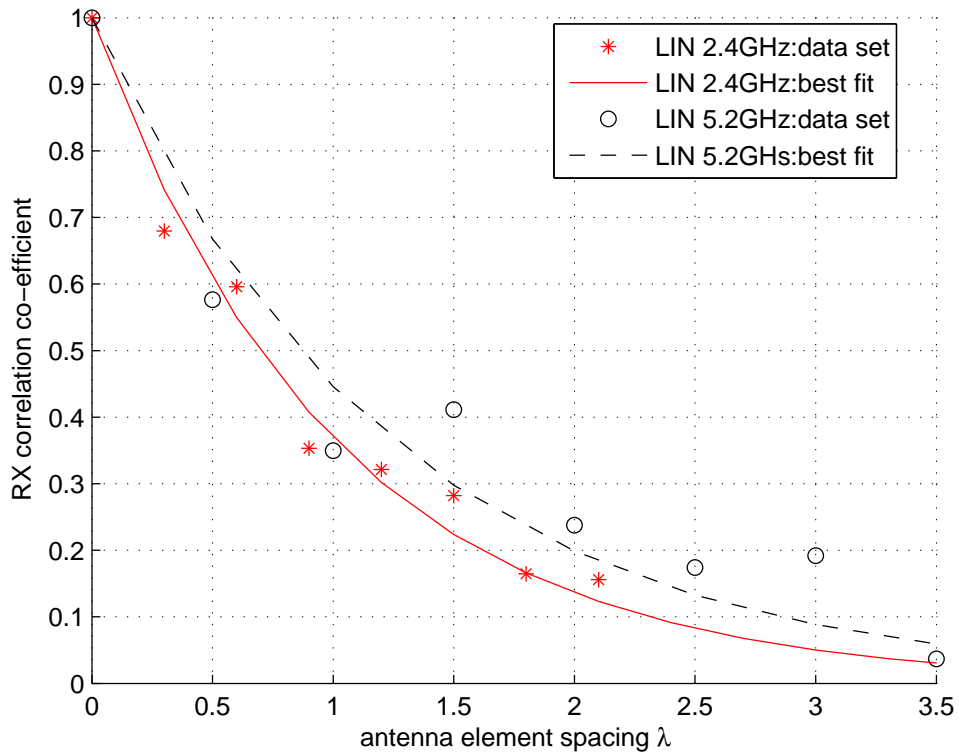


FIGURE 5.13: Calculated relative correlation coefficients with curve fit for RX location 7

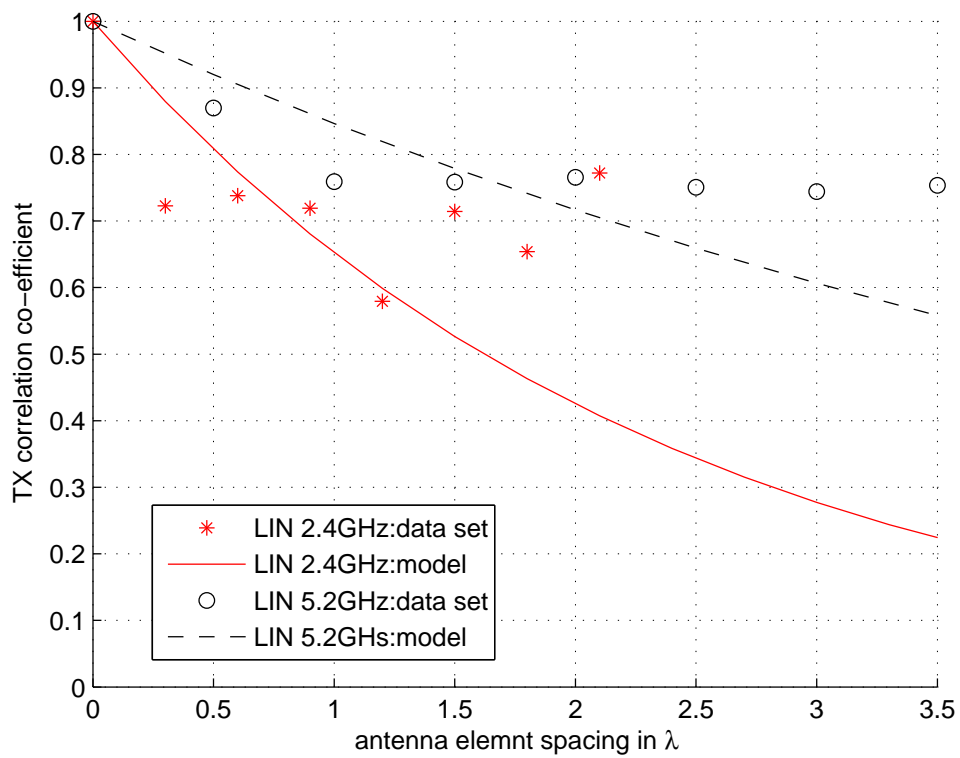


FIGURE 5.14: Calculated relative correlation coefficients with curve fit for TX location 4

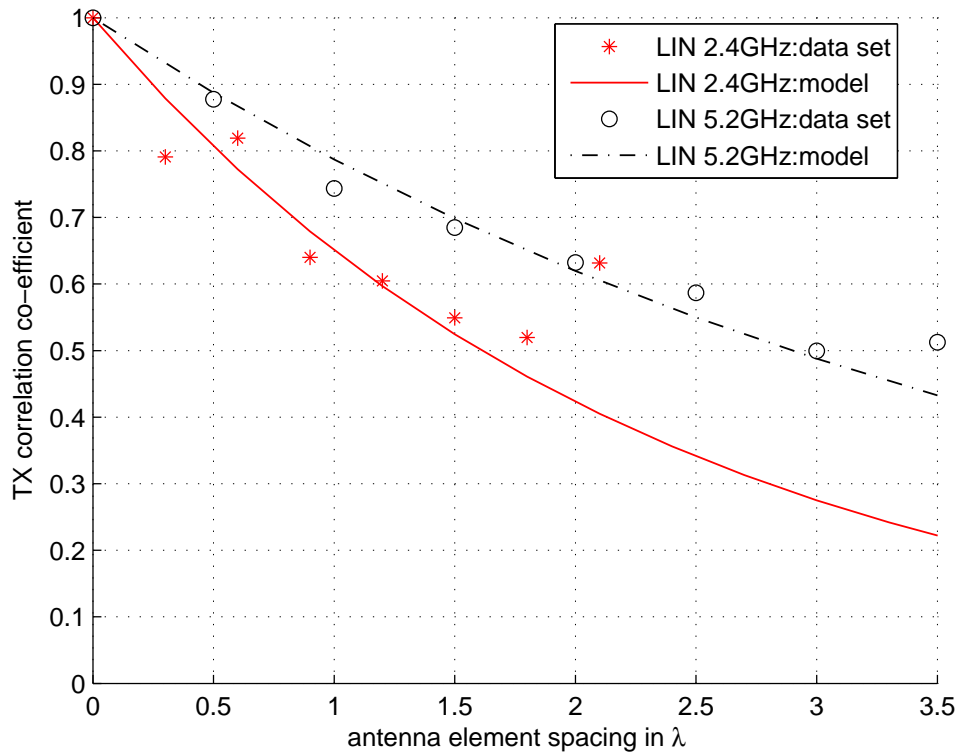


FIGURE 5.15: Calculated relative correlation coefficients with curve fit for TX location 8

TABLE 5.4: Decorrelation Parameter (b) and Error wrt Wavelength ( $\lambda$ ) at RX

Locations	2.4 GHz		5.2 GHz	
	b	error(%)	b	error(%)
1	0.8960	4.76	0.8702	3.27
2	1.0903	4.48	1.2795	1.76
3	1.2546	2.00	1.5591	5.64
4	0.4080	0.75	0.2550	1.06
5	0.8799	3.49	1.0536	2.57
6	0.3182	1.15	0.3432	0.98
7	0.9978	0.17	0.9071	0.72
8	0.4190	0.35	0.4883	1.46
9	1.2042	1.18	0.3442	0.45
10	0.9980	2.90	1.0403	2.40
11	1.5548	3.65	1.9721	5.41

TABLE 5.5: Decorrelation Parameter (b) and Error wrt Wavelength ( $\lambda$ ) at TX

Locations	2.4 GHz		5.2 GHz	
	b	error(%)	b	error(%)
1	0.9511	0.18	0.9769	1.54
2	0.8849	1.69	1.0189	2.66
3	1.0666	2.34	1.2988	1.68
4	0.4270	2.90	0.2400	2.96
5	0.8325	0.06	0.8746	2.08
6	0.6833	0.56	0.7402	5.84
7	1.2678	1.38	1.4634	1.13
8	0.4302	0.84	0.2845	0.51
9	1.6701	0.96	0.3530	1.03
10	1.4210	3.15	1.0134	0.75
11	1.0462	0.76	0.9514	0.49

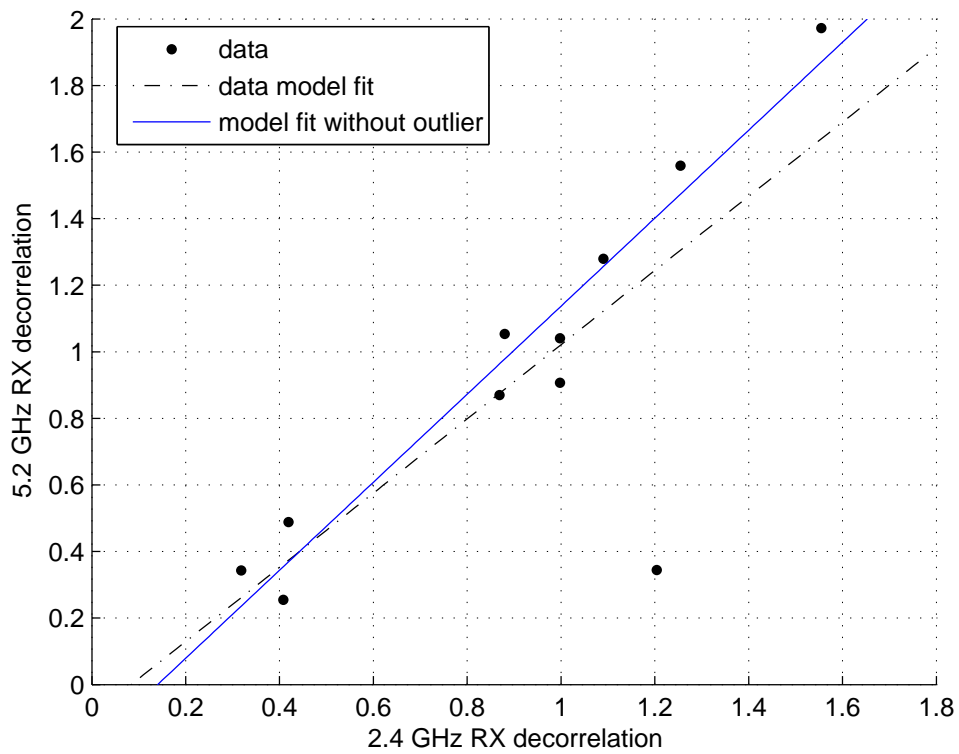


FIGURE 5.16: Relationship of RX decorrelation with respect to frequency scaling

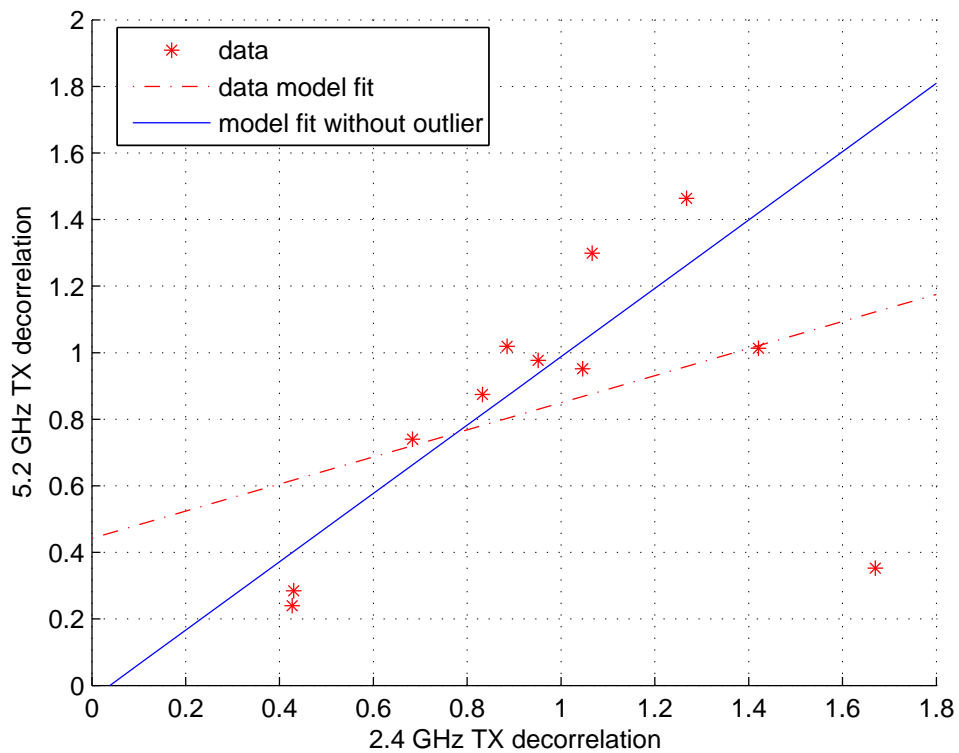


FIGURE 5.17: Relationship of TX decorrelation with respect to frequency scaling



These results show that the correlation at the two frequencies exhibits a strong dependence, suggesting that not only the level of multipath at the frequencies are similar, but also that the directional signature is related as is seen in section 5.3.

## 5.3 DOUBLE DIRECTIONAL CHANNEL MODELLING

### 5.3.1 Introduction

Since initial research in multiple-input-multiple-output (MIMO) wireless systems [9], the opportunities and demands of higher spectral efficiency, quality of service and data rates in wireless systems have stimulated ongoing research in this area. MIMO architectures are potentially good candidates for future wireless systems, since they employ multiple antennas at both the transmitter (TX) and the receiver (RX) to significantly increase channel capacity in a multipath environment, without increasing the system bandwidth or transmit power.

Accurate characterization of the propagation channel is essential in order to assess the potential benefit of employing sophisticated coding, modulation, and antenna arrays in MIMO systems. This is accomplished either by statistical or geometrical modelling, advanced modelling strategies (such as ray tracing) and direct measurement [19]. Modelling approaches have the advantage of inexpensive implementation on a computer, but may lack sufficient accuracy in representing real-world channels. Direct channel measurement provides accurate characterization, but can be time-consuming and expensive, allowing only a small set of communications channels to be investigated. With the advent of technologies such as ultra-wideband (UWB) communications, and the allocation of new RF spectra, channel characterization becomes necessary not only for several different scenarios, but also for many different communication bands.

This chapter explores the effect of center frequency on the MIMO channel response in an indoor environment, showing that in certain cases the double-directional response of the channel at 2.4 GHz is remarkably similar to that at 5.2 GHz, indicating that propagation mechanisms at the two frequencies may also be very similar. Employing measurements at one frequency to predict channel behavior at a different frequency is referred to herein as *frequency scaling*. In theory, this technique can drastically reduce the cost of MIMO channel measurement campaigns



and decrease development time of MIMO systems.

### 5.3.2 Model Description

The antenna arrays employed in this measurement were uniform circular arrays (UCAs) with  $0.5\lambda$  spacing at both 2.4 GHz and 5.2 GHz, where  $\lambda$  is the free-space wavelength. As depicted in Figure 4.21, the RX was placed at 11 different office and laboratory locations, while the TX was placed at a single fixed position in the corridor of CEFIM at the University of Pretoria, South Africa. The RX was set at exactly the same position, height, configuration and direction for both the 2.4 GHz and 5.2 GHz measurements.

At each location, 20 channel snapshots were recorded with 200 ms between snapshots. Since negligible channel variation was observed for each stationary measurement, only a single snapshot from each location was considered. Here, a channel snapshot is defined as  $H_{ij}^{(k)}$ , where  $k$  is a frequency bin index, and  $i$  and  $j$  are the receive and transmit antenna indices respectively. To remove the effect of path loss in our computations, channel matrices were normalized to have average unit SISO gain, as indicated in [95].

Previous channel modelling efforts have defined the double-directional channel [17] in terms of paired discrete plane-wave departures and arrivals at the TX and RX. In indoor environments, where multipath scattering is severe, extracting individual plane-wave arrivals can be very difficult. It was therefore decided to define the double-directional response in terms of spatial power spectra, obtained with either joint TX/RX Bartlett or Capon beamformers [42]. The joint Capon beamformer can now therefore be defined as

$$P_{\text{CAP}}(\nu_T, \nu_R) = \frac{1}{\mathbf{a}(\nu_T, \nu_R)^H \hat{\mathbf{R}}^{-1} \mathbf{a}(\nu_T, \nu_R)}, \quad (5.12)$$

where  $\{\cdot\}^H$  is complex conjugate transpose,  $\nu_T$  and  $\nu_R$  are azimuth angles at the TX and RX, and  $\hat{\mathbf{R}}$  is the sample covariance matrix. The joint steering vector  $\mathbf{a}(\nu_T, \nu_R)$  is defined as

$$\mathbf{a}(\nu_T, \nu_R) = \mathbf{a}_T(\nu_T) \otimes \mathbf{a}_R(\nu_R), \quad (5.13)$$



where  $\mathbf{a}_{\{T,R\}}$  are the usual separate array steering vectors for the TX and RX, and  $\otimes$  is the Kronecker product. The sample covariance matrix is computed as

$$\hat{\mathbf{R}} = \frac{1}{K} \sum_k \mathbf{h}^{(k)} \mathbf{h}^{(k)H}, \quad (5.14)$$

where  $K$  is the total number of frequency bins,  $\mathbf{h}^{(k)} = \text{Vec} \{ \mathbf{H}^{(k)} \}$ , and the vector operation  $\text{Vec} \{ \cdot \}$  stacks a matrix into a vector.

Likewise, the joint Bartlett beamformer is defined as

$$P_{\text{BF}}(\nu_T, \nu_R) = \frac{\mathbf{a}(\nu_T, \nu_R)^H \hat{\mathbf{R}} \mathbf{a}(\nu_T, \nu_R)}{\mathbf{a}(\nu_T, \nu_R)^H \mathbf{a}(\nu_T, \nu_R)} \quad (5.15)$$

The similarity of the spectra at 2.4 GHz and 5.2 GHz is evaluated by computing the correlation coefficient on the double-directional spectra at the two different frequencies using either the Capon or Bartlett beamformer. The correlation coefficient is computed as

$$\rho = \frac{\sum_{j=0}^N \sum_{i=0}^N (P_{2.4,ij} - \bar{P}_{2.4})(P_{5.2,ij} - \bar{P}_{5.2})}{\sqrt{\left[ \sum_{i=0}^N \sum_{j=0}^N (P_{2.4,ij} - \bar{P}_{2.4})^2 \right] \left[ \sum_{i=0}^N \sum_{j=0}^N (P_{5.2,ij} - \bar{P}_{5.2})^2 \right]}}, \quad (5.16)$$

where  $N$  is the number of discretization points,  $P_{f,ij} = P_{\{\text{CAP,BF}\}}(\nu_{T,i}, \nu_{R,j})$ ,  $f$  is the center frequency in GHz,  $\nu_{T,i} = \nu_{R,i} = 2\pi i/N$ , and  $\bar{P}_f = (1/N^2) \sum_i \sum_j P_{f,ij}$ .

### 5.3.3 Results

Figures 5.18 and 5.19 shows the joint spatial power spectra at Location 4 for the Bartlett and Capon beamformers.

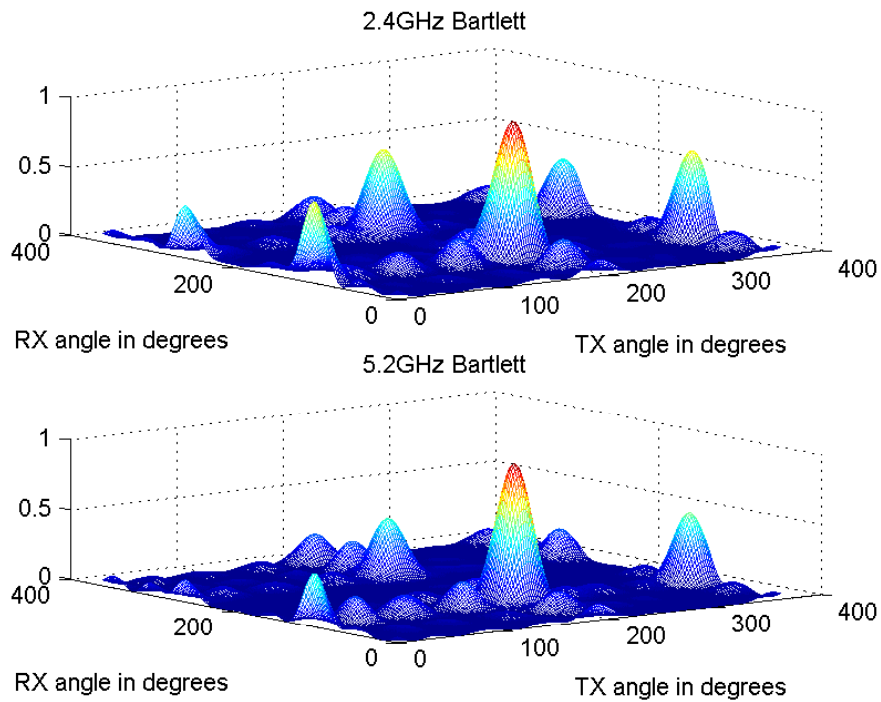


FIGURE 5.18: Spatial spectra for Location 4 employing the Bartlett Beamformer

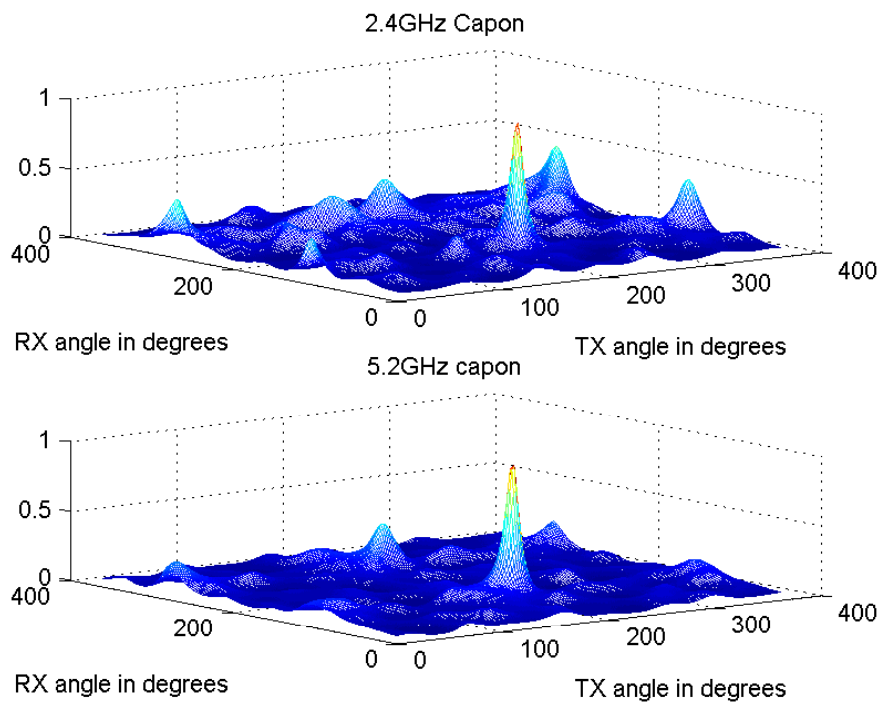


FIGURE 5.19: Spatial spectra for Location 4 employing the Capon Beamformer



TABLE 5.6: Correlation coefficient of 2.4 GHz and 5.2 GHz spectra

Locations	Bartlett Beamformer	Capon Beamformer
	$\rho_{BF}$	$\rho_{CAP}$
1	0.37	0.73
2	0.56	0.77
3	0.43	0.72
4	0.56	0.94
5	0.62	0.59
6	0.58	0.47
7	0.35	0.56
8	0.51	0.76
9	0.33	0.56
10	0.25	0.16
11	0.41	0.63

One observes that there is a similarity in the spatial structure of the electromagnetic waves for both beamforming techniques. An alternate approach shown in Figures 5.20 and 5.21 shows the contour mapping of the power spectra also for Location 4 at 2.4 GHz and 5.2 GHz respectively. This is verified by the respective correlation coefficient of 0.56 (Bartlett) and 0.94 (Capon) shown in Table 5.6. Where the joint correlation coefficient shown in Table 5.6, is relatively lower (such as Location 7), one would expect the geometry of the power spectra to be different. This is the case as observed in Figures 5.22 and 5.23, where the angular positions may be somewhat similar, but the amplitudes differ. The plots also indicate that the Bartlett beamformer performs better in terms of spatial similarity, and this is congruent with the higher correlation coefficient computed.

As depicted in Figures 5.24 and 5.25, Location 11 has more scattering but still exhibits a high degree of correlation in the spectra for either beamforming technique. Table 5.6 indicates that the Capon beamformer usually produces a higher correlation coefficient than the Bartlett beamformer, with the exception of Locations 6 and 10. This result might be expected, since the Bartlett beamformer tends to produce complicated interference patterns between major scattering directions, but the Capon beamformer often suppresses this effect. Thus, although

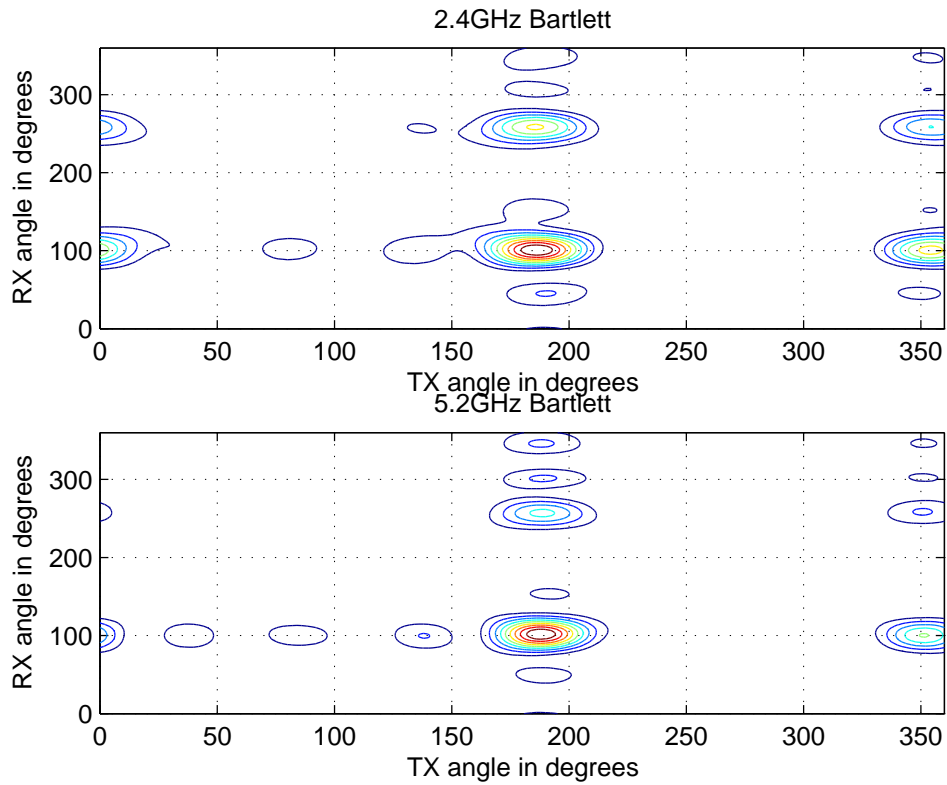


FIGURE 5.20: Spectral contour for Location 4 employing the Bartlett Beamformer

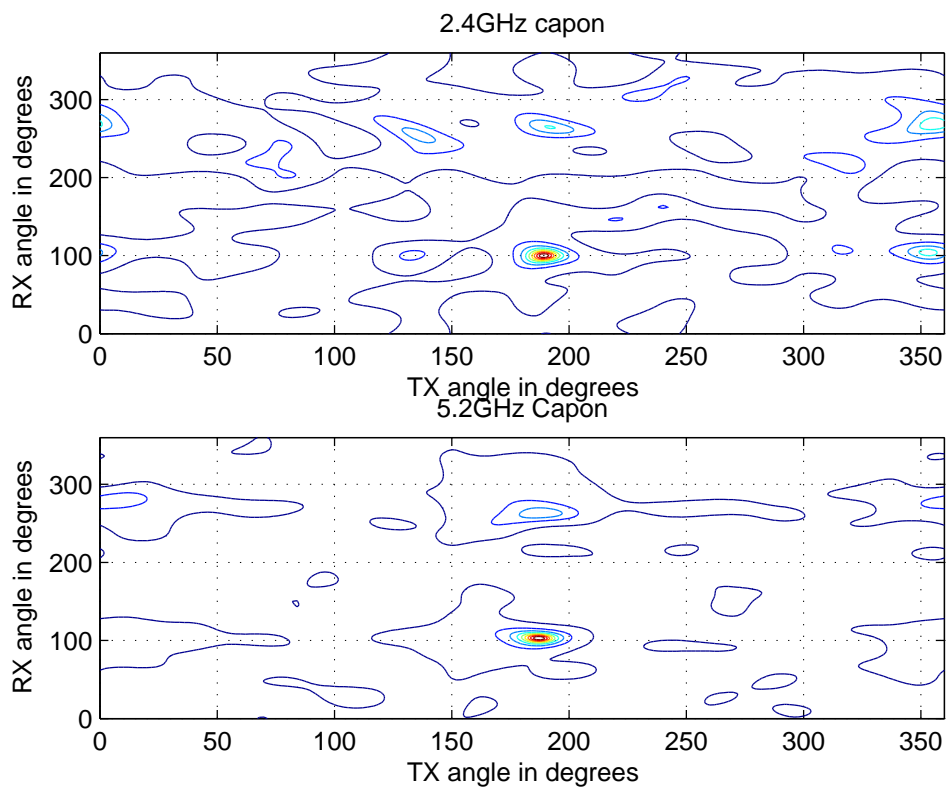


FIGURE 5.21: Spectral contour for Location 4 employing the Capon Beamformer

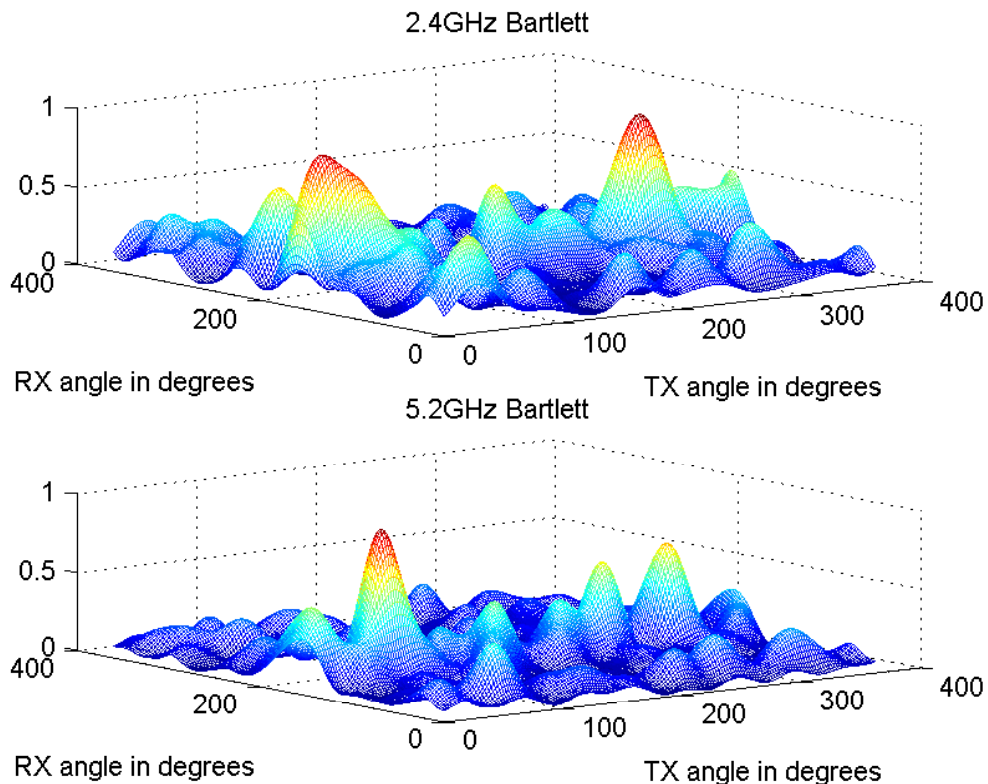


FIGURE 5.22: Spatial spectra for Location 7 employing the Bartlett Beamformer

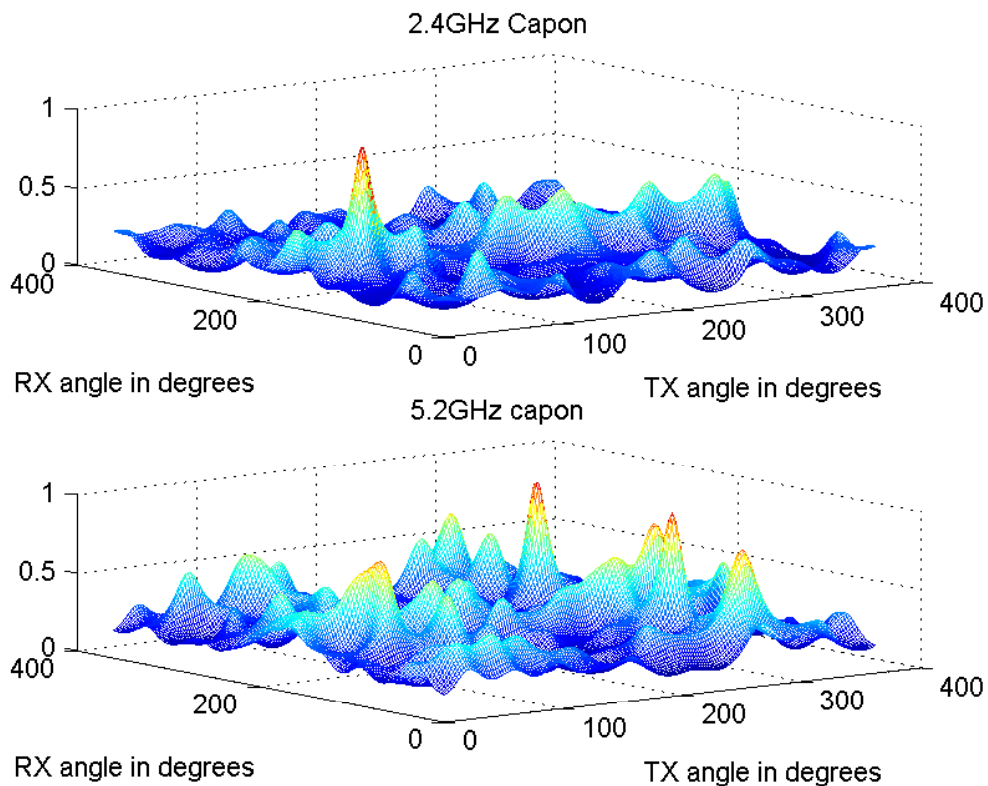


FIGURE 5.23: Spatial spectra for Location 7 employing the Capon Beamformer

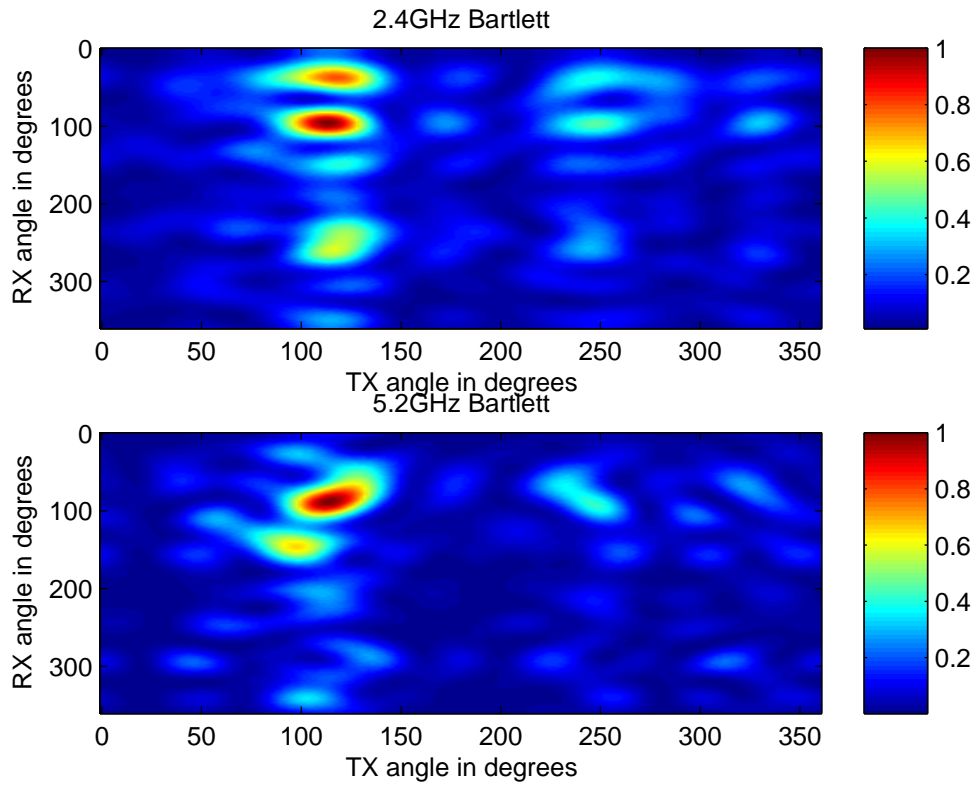


FIGURE 5.24: Spatial spectra for Location 11 employing the Bartlett Beamformer

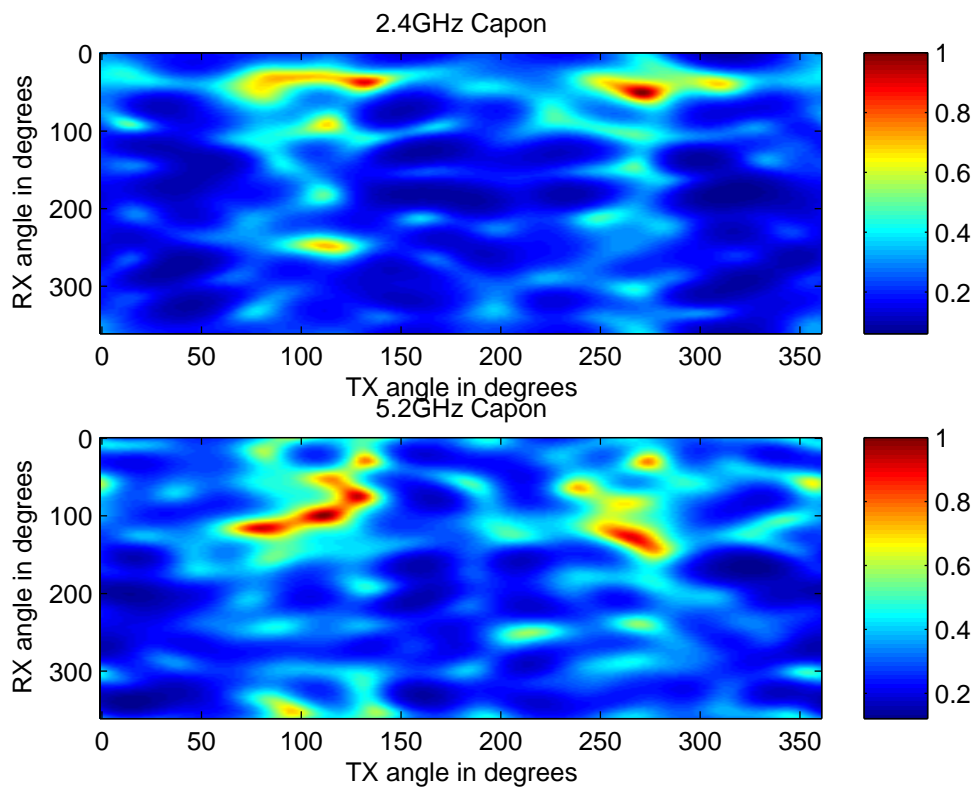


FIGURE 5.25: Spatial spectra for Location 11 employing the Capon Beamformer



the Bartlett beamformer may be a more sensitive metric for comparison of joint spatial power spectra, the Capon beamformer will focus on comparing the principal directions of arrival and departure.

## 5.4 CONCLUSION

### 5.4.1 Capacity Modelling

A study on the effect of frequency scaling on capacity in indoor MIMO wireless systems has been presented. The results for the circular antenna array configuration suggest that one can predict the capacity in a MIMO system at another center frequency through a linear dependence relationship. The pairwise correlation coefficient presented can also be reliably used as a metric to explain the differences in measured capacities at the various locations.

### 5.4.2 Spatial Correlation

Through the study of the spatial correlation for a ULA at both 2.4 GHz and 5.2 GHz it has been shown that for an indoor office type environment there can be exploitation of the relationship of the correlation in MIMO wireless systems. Furthermore, the model determined through the measurement campaign confirmed the model that is sometimes used in the literature [98]. Measured capacity for the ULA at 2.4 GHz and 5.2 GHz suggests that one can predict the correlation through a linear dependence relationship. This suggests that there is high correlation in the directional signature of the multipath propagation. These results suggest that propagation mechanisms in the indoor environment at these two distinct carrier frequencies may be very similar, leading to cost savings in channel measurement campaigns, network planning and MIMO system development.

### 5.4.3 Double Directional Channel

The idea of frequency scaling in the double-directional joint TX/RX case, or using measured channel characteristics at one center frequency to predict behavior at another frequency, have been proposed. This could save time and cost of channel characterization and network planning. The ability to perform frequency scaling was investigated by comparing the double-directional spectra of measured indoor channels at 2.4 GHz and 5.2 GHz. Comparison of the spatial spectra



at the two center frequencies showed a high degree of similarity, suggesting that the multipath propagation at the two frequencies is mainly due to specular reflections. These results are promising, since it suggests that models may be developed that predict channel behavior at many different bands given measurements at only a single center frequency.